Available online at www.sciencedirect.com
ScienceDirect
Trans. Nonferrous Met. Soc. China 33(2023) 2574−2587
Transactions of Nonferrous Metals Society of China
www.tnmsc.cn

Low cycle fatigue behavior and fatigue life prediction of 2195 Al−Li alloy at warm temperatures

Zi-jie MENG[1], Cun-sheng ZHANG[1], Cheng-ge WU[2], Hao ZHANG[3], Liang CHEN[1], Guo-qun ZHAO[1], Hai YAN[2]

1. Key Laboratory for Liquid-Solid Structural Evolution & Processing of Materials (Ministry of Education), Shandong University, Jinan 250061, China;
2. School of Construction Machinery, Shandong Jiaotong University, Jinan 250357, China;
3. Jiangsu Haoran Spray Forming Alloy Co., Ltd., Zhenjiang 212009, China

Received 10 March 2022; accepted 29 August 2022

Abstract: The strain-controlled low cycle fatigue (LCF) tests were firstly carried out to investigate the LCF behavior of the 2195 Al−Li alloy at warm temperatures (100 and 200 °C). All initial and mid-life hysteresis loops showed a centrosymmetric characteristic. The cyclic stress response curve at 100 °C and strain of 0.6% exhibited complete cyclic hardening, while response curves under other conditions showed cyclic hardening initially followed by cyclic softening. Then, various fatigue life prediction models were employed to evaluate LCF life. The prediction model based on the total strain energy density could present the best prediction accuracy. Finally, the fatigue fracture under different conditions was observed to reveal the fatigue fracture mechanism. The fatigue striations were visible at 100 °C and strain of 0.6%, but gradually diminished with increasing temperature and strain. Furthermore, the fatigue fracture zone at 200 °C and strain of 1.0% presented an evident intergranular fracture characteristic.

Key words: 2195 Al−Li alloy; low cycle fatigue behavior; fatigue life prediction; fatigue fracture behavior

1 Introduction

Compared with traditional aluminum alloys, Al−Li alloys have attracted extensive attention in the aerospace field due to their low density, high specific strength, and good fatigue resistance [1−3]. Al−Li alloys are generally used to manufacture the essential structural components [4−6], which are frequently subjected to complicated temperature fields and fluctuating loads in service. As a result, the fatigue life or behavior of Al−Li alloys is an important factor that should be considered in engineering design.

XU et al [7] investigated the fatigue behavior of an Al−Cu−Li alloy at ambient and cryogenic temperatures and found that the fatigue strength increased as the testing temperature decreased. ZHANG et al [8] investigated the low cycle fatigue performance of 2195 Al−Li alloy at ambient temperature, and it was found that the cyclic properties of the alloy were closely related to the interactions between dislocations, grain boundaries, and second phase particles. PRASAD and RAO [9] studied the low cycle fatigue (LCF) behavior of several Al−Li alloys at room temperature and pointed out that the fatigue resistance of the alloys was closely related to the alloy composition, aging state, and microstructure. LIU and WANG [10] investigated the low cycle fatigue behavior of 8090 Al−Li alloy. It was observed that the heat-treated alloy showed cyclic hardening followed by cyclic softening characteristics, whereas the alloy exhibited a continuous cyclic softening behavior after equal

Corresponding author: Cun-sheng ZHANG, Tel: +86-531-88392811, E-mail: zhangcs@sdu.edu.cn;
Cheng-ge WU, Tel: +86-531-80687523, E-mail: chgwu2002@163.com
DOI: 10.1016/S1003-6326(23)66282-X

angular extrusion. LEWANDOWSKA et al [11] considered that the existence of T_1 phases could lead to more uniform plastic deformation and significantly improve the fatigue resistance of Al−Li alloys at ambient temperature.

It is generally accepted that the fatigue property is closely related to the loading temperature [12]. From the above reviews, the fatigue behavior of Al−Li alloys at room temperature has been systematically reported. Besides, an amount of research has already been carried out on the high cycle fatigue properties, fatigue crack growth behavior, and fatigue behavior of friction stir welded joints of Al−Li alloys [13−20]. However, the reasonable characterization on the LCF behavior of the 2195 Al−Li alloy at warm temperatures has never been illustrated yet.

The fatigue life prediction is of great significance for the practical application of Al−Li alloy components, so it is dispensable to develop efficient life prediction models with high prediction accuracy. GANESH SUNDARA RAMAN and RADHAKRISHNAN [21] combined the Coffin−Manson and Basquin models with the cyclic stress−strain relation for low cycle fatigue analysis. KLIMAN and BÍLÝ [22] pointed out that the plastic strain energy density could be employed as an essential parameter for predicting the fatigue life. GOLOS and ELLYIN [23] proposed a unified theory based on total strain energy density and revealed that damage parameters based on total strain energy density could be used to characterize the low cycle fatigue failure and cumulative damage processes. WANG et al [24] proposed a fatigue life prediction model based on strain rate optimized hysteresis energy, which took both fatigue and creep damage into account. ZHANG et al [25] developed a novel LCF life prediction model that took grain size into account, discovering that the prediction accuracy of the new model outperformed the Manson−Coffin relationship and the Ostergren energy method.

As a typical third-generation Al−Li alloy, 2195 Al−Li alloy used in this work has been successfully applied to aircraft wings and fuel tanks [26−29]. For the supersonic aircraft, when its flight speed exceeds Mach 2, the aerodynamic heating effect (air compression leads to an increasing temperature for aircraft) could not be neglected. It is found that when the aircraft speed reaches Mach 2 and Mach 2.5, the corresponding temperature of aircraft is roughly 117 and 210 °C. In addition, the high temperature generated by the aerodynamic heating effect makes the thin-walled components such as space shuttle wings and skin vibrate with the fixed frequency and amplitude, thus causing instability of these structures and even endangering the safety of aircraft.

Therefore, the LCF behavior and fatigue life prediction of 2195 Al−Li alloy at warm temperatures were investigated in this work, which is similar to the fixed-frequency vibration behavior caused by the aerodynamic heating in supersonic aircraft flying at Mach 2 and Mach 2.5. The low cyclic fatigue test was first carried out at warm temperatures (100 and 200 °C) and the cyclic stress response behavior was analyzed. Meanwhile, the fatigue life of the 2195 Al−Li alloy was predicted based on different models. Finally, the fatigue fracture morphology of the alloy was observed to illustrate the fatigue fracture mechanism.

2 Experimental

2.1 Material preparation

The test material used in this work is an extruded 2195 Al−Li alloy sheet prepared by spray-forming, and its chemical composition is indicated in Table 1. Firstly, a cylindrical billet with the specification of *d*550 mm × 800 mm was obtained by the spray forming process. A schematic diagram of the spray forming device is shown in Fig. 1(a). Then, the hot extrusion was performed on a 100 MN extrusion press with an extrusion speed of 0.1 mm/s, die temperature of 450 °C, and billet temperature of 470 °C. Finally, a rectangular sheet with a size of 710 mm × 500 mm × 20 mm was acquired. After the extrusion, the sheet was treated with a 2 h solid solution at 505 °C, followed by quenching in water, and subsequently, a 6 h artificial aging treatment at 170 °C, as illustrated in Fig. 1(b).

Table 1 Chemical composition of spray-formed 2195 Al−Li alloy (wt.%)

Cu	Li	Mg	Ag	Zr	Fe	Al
4.02	0.92	0.49	0.36	0.12	0.066	Bal.

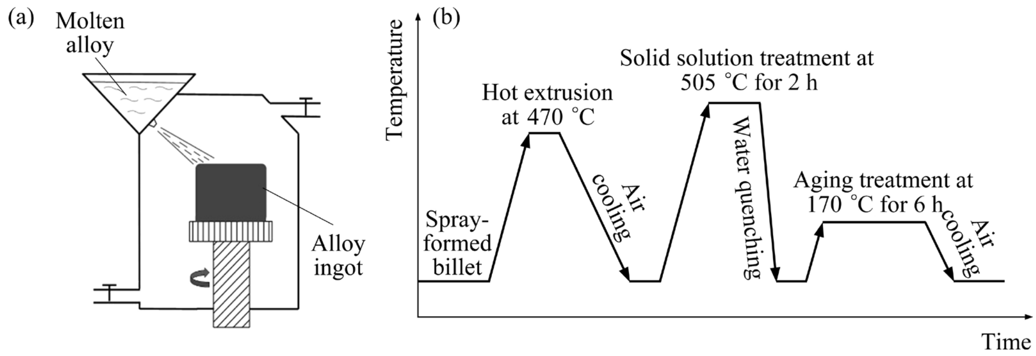

Fig. 1 Schematic diagram of spray forming device (a) and heat treatment route of alloy (b)

2.2 LCF tests

LCF sample preparation and experiments were carried out according to ISO 12106:2017. Each fatigue sample was taken along the extrusion direction from the central plane of the extrusion billet. The sample dimensions are presented in Fig. 2. Tension−compression loading LCF tests with a strain-controlled symmetric triangular waveform were conducted on an MTS 370 testing machine at total strains ranging from 0.5% to 1.0%, corresponding to loading frequencies ranging from 0.45 to 0.2 Hz, as shown in Table 2, and the test temperatures were 100 and 200 °C, respectively. In the process of LCF tests, the furnace of the LCF machine was set to be a given experimental temperature firstly, and then the fatigue specimen was placed into the furnace. The heating time of each specimen was set to be 20 min and then held for 30 min after reaching the experimental temperature. LCF samples were subjected to cyclic loading until final rupture.

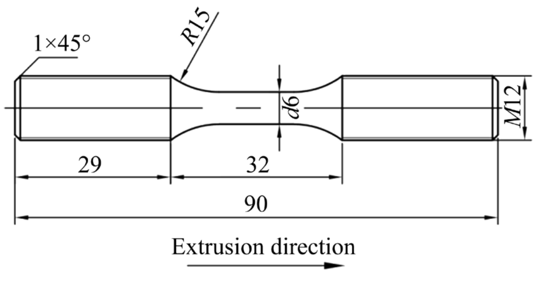

Fig. 2 Dimensions of LCF samples (unit: mm)

Table 2 Strains and loading frequencies in LCF tests

Strain /%	0.5	0.6	0.7	0.8	1.0
Loading frequency/Hz	0.45	0.4	0.35	0.3	0.2

2.3 Microstructure characterization

To analyze the effect of temperature and strain on the fracture behavior, the fracture morphology of the alloy was observed by a JSM−6610LV scanning electron microscope (SEM). All SEM samples were cut within a gauge length of approximately 7 mm away from the fracture position.

3 Results

3.1 LCF behavior

3.1.1 Hysteresis loops

Figure 3 shows the initial cycle (IC) and mid-life cycle (MC) hysteresis loops at different temperatures (100 and 200 °C) and strains (0.5%, 0.6%, 0.7%, 0.8%, and 1.0%), respectively. It is noted that the area enclosed by the hysteresis loops represents the degree of plastic deformation of materials. It can be seen that all hysteresis loops exhibited centrosymmetric characteristics, which indicated that the cyclic deformation behavior of the alloy under the tensile and compressive stages of cyclic loading was nearly identical. In addition, with increasing the strain, the area of hysteresis loops at various temperatures increased, revealing that more plastic deformation occurred with increasing the strain.

Figure 4 shows the comparison of initial and mid-life hysteresis loops at different temperatures and total strains of 0.5%, 0.7%, and 1.0%, respectively. At the total strain of 0.5%, the IC and MC hysteresis loops at 100 °C were quite narrow, and the shape of curves was approximately a straight line, indicating that the fatigue damage under this condition was minor or negligible. However, the hysteresis loop at 200 °C became a

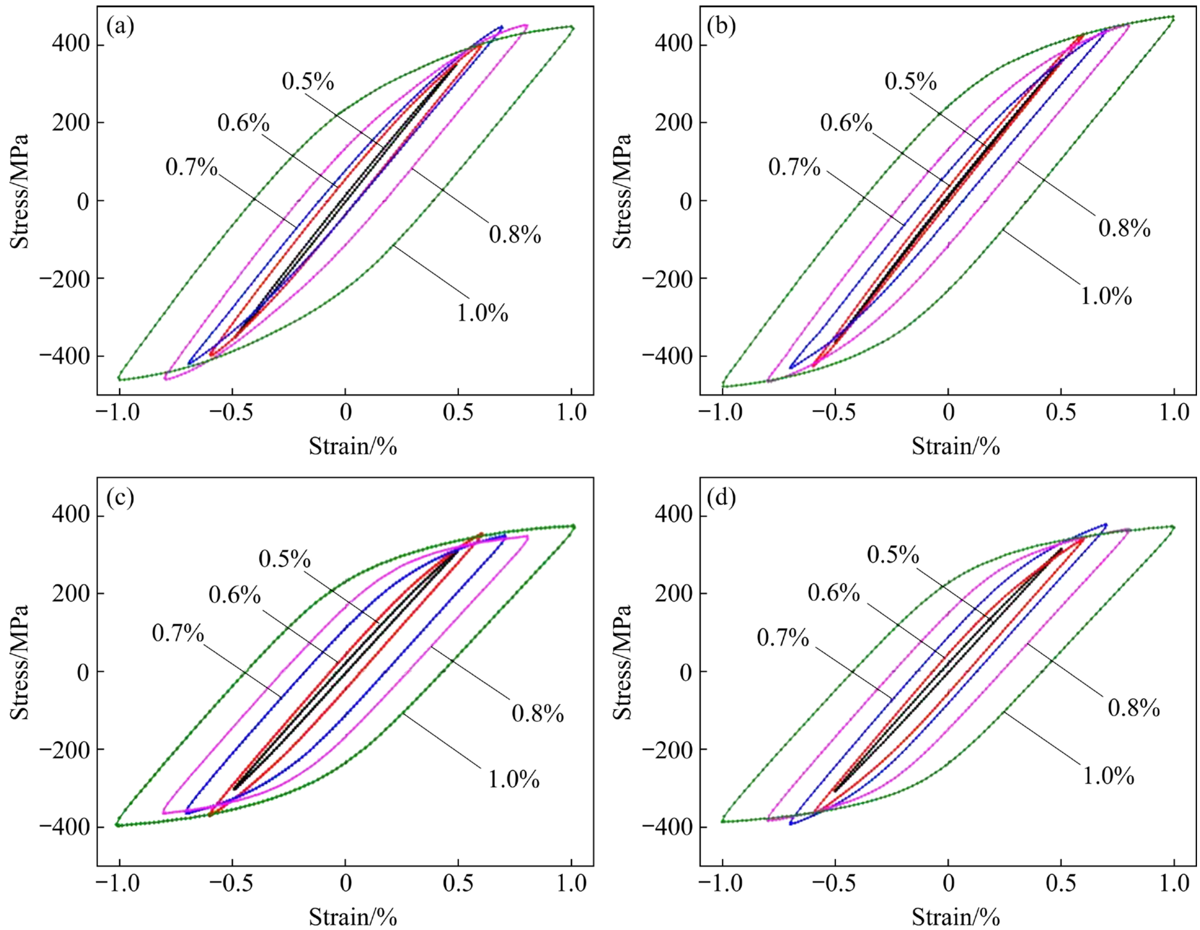

Fig. 3 Stress−strain hysteresis loops of initial (a, c) and mid-life (b, d) cycles at different temperatures: (a, b) 100 °C; (c, d) 200 °C

certain area, suggesting that plastic strain was generated during the cyclic loading. With increasing strain to higher degrees (0.7% and 1.0%), the area of IC and MC hysteresis loops at various temperatures gradually increased, and the bending degree near the peak stress end of IC and MC hysteresis loops was more obvious. It was revealed that with an increase of total strain, the degree of plastic deformation increased continuously, and the yield behavior also became more noticeable. Furthermore, the cyclic stress of IC and MC hysteresis loops at 200 °C was lower than that at 100 °C and all strains.

3.1.2 Cyclic stress response behavior

Generally, the cyclic stress varies with the strain in a cyclic loading process. If the cyclic stress increases continuously with the cyclic loading, it is called cyclic hardening, otherwise, it is called cyclic softening [30]. Under specific conditions, the cyclic stress response behavior of a material is related to its heat treatment state [31].

The cyclic stress response curves under different strains and temperatures are given in Fig. 5. The cyclic stress of the alloy at 100 °C was higher than that at 200 °C with the same strain. As the strain increased, the cyclic stress of the alloy at the same temperature increased and fatigue life decreased. At the total strain of 0.5%, a slight cyclic hardening of the alloy at 100 °C was observed at the initial stage of cyclic loading, followed by a slow decrease in cyclic stress after about 4000 cycles, which exhibited quite weak cyclic softening until final fatigue fracture. When the temperature increased to 200 °C, the initial cyclic hardening and subsequent cyclic softening were also observed. However, the cyclic softening rate increased dramatically after about 3500 cycles until the final fracture. At the total strain of 0.6%, the alloy at 200 °C presented a slight cyclic hardening followed by an obvious cyclic softening whereas the material at 100 °C exhibited complete cyclic hardening characteristics throughout the entire fatigue life.

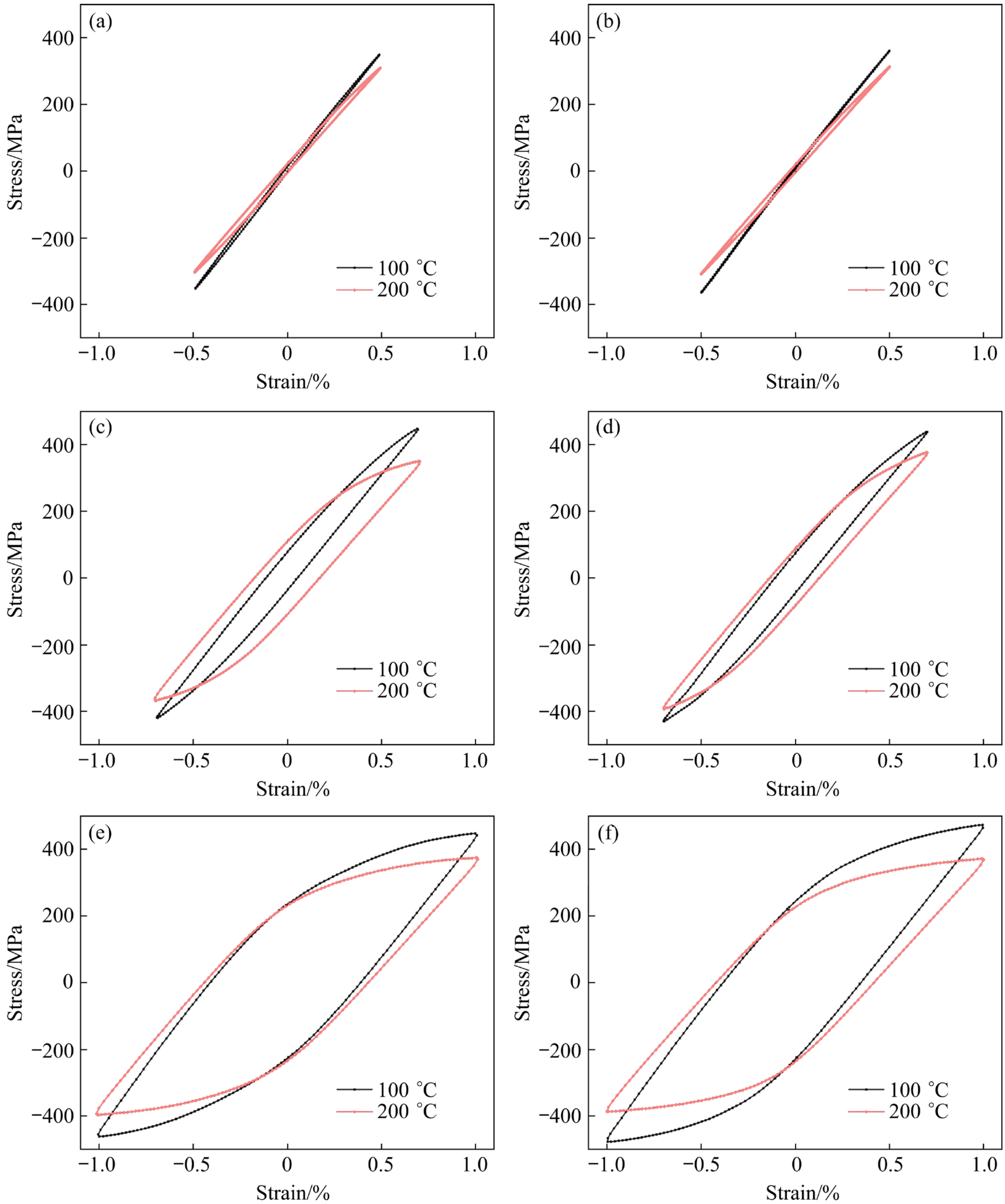

Fig. 4 Comparison of initial (a, c, e) and mid-life (b, d, f) hysteresis loops at different temperatures and strains: (a, b) 0.5%; (c, d) 0.7%; (e, f) 1.0%

When the total strain increased to higher levels (0.7% and 0.8%), the cyclic stress response behavior of the alloy at 100 and 200 °C was quite similar, displaying cyclic hardening initially and subsequently cyclic softening throughout the whole fatigue life, and a rapid decrease in the cyclic stress at the cyclic softening stage. However, at the cyclic hardening stage, the cyclic stress increased slightly at 100 °C, whereas the cyclic stress increased substantially at 200 °C. As the total strain rose to 1.0%, the alloy at different temperatures exhibited a slight increase in the cyclic stress at the cyclic hardening stage, while at the cyclic softening stage, the cyclic stress at 200 °C decreased more significantly than that at 100 °C, demonstrating a more obvious cyclic softening characteristic.

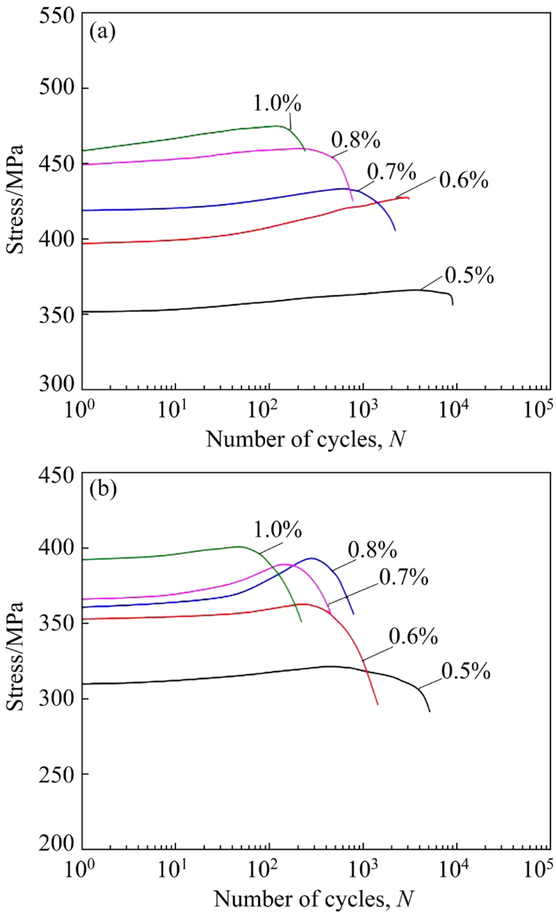

Fig. 5 Cyclic stress response curves at different strains and temperatures: (a) 100 °C; (b) 200 °C

3.2 Low cycle fatigue life prediction

The relation between cyclic stress and total strain of 2195 Al−Li alloy can be characterized by the following formula:

$$\frac{\Delta\varepsilon_t}{2}=\frac{\Delta\varepsilon_e}{2}+\frac{\Delta\varepsilon_p}{2}=\frac{\Delta\sigma}{2E}+\left(\frac{\Delta\sigma}{2K'}\right)^{1/n} \tag{1}$$

where E is Young's modulus of the material, K' is the cyclic strength coefficient, n is the cyclic hardening index, $\Delta\sigma/2$ is the cyclic stress, $\Delta\varepsilon_e/2$, $\Delta\varepsilon_p/2$ and $\Delta\varepsilon_t/2$ represent the elastic strain, the plastic strain, and the total strain, respectively. Meanwhile, Eq. (1) can be decomposed further into the relation of cyclic stress versus plastic strain and elastic strain, as illustrated in Eqs. (2) and (3), respectively. The values of E, K', and n at different temperatures are acquired by linear regression analysis, as given in Table 3.

$$\frac{\Delta\sigma}{2}=K'\left(\frac{\Delta\varepsilon_p}{2}\right)^n \tag{2}$$

$$\frac{\Delta\sigma}{2}=E\frac{\Delta\varepsilon_e}{2} \tag{3}$$

3.2.1 Low-cycle fatigue life prediction based on total strain

In the strain-controlled low-cycle fatigue test, the total strain is a critical factor in determining the fatigue life of materials and it is composed of elastic strain and plastic strain. The Basquin and Coffin−Manson model expressions based on the relation of fatigue life in terms of elastic and plastic strains are presented in Eqs. (4) and (5), respectively. By combining the aforementioned equations, the Coffin−Manson−Basquin(CMB) fatigue life prediction model related to the total strain can be obtained, as shown in Eq. (6).

$$\frac{\Delta\varepsilon_e}{2}=\frac{\sigma_f'}{E}(2N_f)^b \tag{4}$$

$$\frac{\Delta\varepsilon_p}{2}=\varepsilon_f'(2N_f)^c \tag{5}$$

$$\frac{\Delta\varepsilon_t}{2}=\frac{\Delta\varepsilon_e}{2}+\frac{\Delta\varepsilon_p}{2}=\frac{\sigma_f'}{E}(2N_f)^b+\varepsilon_f'(2N_f)^c \tag{6}$$

where σ_f' and b are the fatigue strength coefficient and exponent, respectively, ε_f' and c are the fatigue ductility coefficient and fatigue ductility exponent, respectively, and N_f is the fatigue life of materials. The fitting values of the above LCF parameters are shown in Table 3.

Relations between total strain and the number of reversals to failure based on the CMB model are presented in Fig. 6(a). It was shown that the fitting curves at 200 °C were closer to the corresponding data points than those at 100 °C. In order to accurately evaluate the reliability of

Table 3 Parameters in fatigue life prediction models for 2195 Al−Li alloy at warm temperatures

t/°C	E/GPa	K'/MPa	n	b	σ_f'/MPa	c	ε_f'	W_f'/(MJ·m^{-3})	β	K/(MJ·m^{-3})	a
100	72.942	503.498	0.057	−0.0636	714.7722	−1.2025	956.7532	13093.3272	−1.2739	75.8122	−0.4474
200	65.189	403.776	0.061	−0.0614	563.4509	−1.0003	216.1623	4593.5488	−1.0675	325.4468	−0.6324

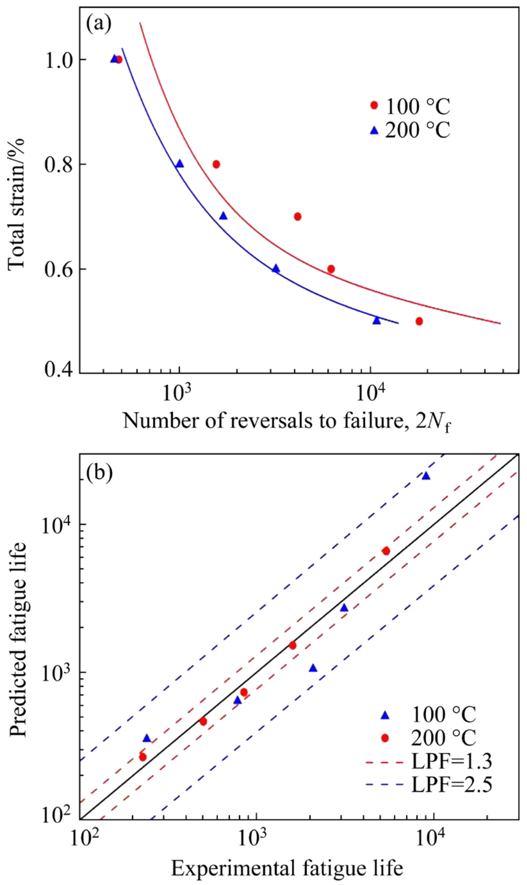

Fig. 6 Relations between total strain and number of reversals to failure based on CMB model at different temperatures (a) and comparison between predicted and experimental fatigue life based on CMB model (b)

different fatigue life prediction models, the fatigue life prediction factor (LPF) was introduced in this work, which could be given as

$$\mathrm{LPF}=\left\{\frac{N_{\mathrm{pre}}}{N_{\mathrm{exp}}},\frac{N_{\mathrm{exp}}}{N_{\mathrm{pre}}}\right\}_{\max} \tag{7}$$

where N_{exp} is the experimental fatigue life, and N_{pre} is the fatigue life predicted by models.

A comparison between predicted and experimental fatigue life based on the CMB model is given in Fig. 6(b). The solid diagonal line indicated the predicted fatigue life was in perfect agreement with experimental fatigue life, while red and blue dashed lines represented the boundaries with LPF values of 1.3 and 2.5, respectively. It was shown that data points at 200 °C were much closer to the diagonal line than those at 100 °C, meaning that the CMB model could offer a more accurate prediction for the fatigue life at a higher temperature.

3.2.2 Low-cycle fatigue life prediction based on plastic strain energy density

Fatigue damage of the material is a process of energy dissipation in essence [32]. For strain-controlled LCF tests, the plastic strain has a significant effect on the fatigue life of materials. Despite the widespread use of the CMB model, the effect of cyclic stress and plastic strain on fatigue life is not taken into consideration. Therefore, the life prediction model based on plastic strain energy density is proposed, which simultaneously considers the effects of cyclic stress and plastic strain on fatigue life. According to previous studies [32−34], the Halford−Marrow (HW) model based on plastic strain energy density was used in this work to conduct fatigue life prediction, as expressed in Eq. (8):

$$\Delta W_{\mathrm{p}}=W_{\mathrm{f}}'(2N_{\mathrm{f}})^{\beta} \tag{8}$$

where W_{f}' and β are the plastic strain energy density coefficient and exponent, respectively, and their fitting values are given in Table 3. ΔW_{p} is the plastic strain energy density of the material in each cycle and its calculation method is shown in Eq. (9):

$$\Delta W_{\mathrm{p}}=\frac{1-n'}{1+n'}\Delta\sigma\Delta\varepsilon_{\mathrm{p}} \tag{9}$$

where n' is the cyclic hardening exponent, $\Delta\sigma$ and $\Delta\varepsilon_{\mathrm{p}}$ are the cyclic stress range and plastic strain range, respectively.

The ΔW_{p}−$2N_{\mathrm{f}}$ relation on the logarithm scale based on the HW model is given in Fig. 7(a), revealing that the fatigue life at various temperatures increases with a decrease in plastic strain energy density. Moreover, fitting curves at 200 °C were also closer to the associated experimental data points than those at 100 °C, which is consistent with the observed result shown in Fig. 6(a). A comparison between predicted and experimental fatigue lives based on the HW model is presented in Fig. 7(b). At 100 and 200 °C, the LPF values of the HW model were smaller than those of the CMB model, marked 2.0 and 1.2, respectively. Therefore, compared with the CMB model, the HW model had a better prediction effect for the fatigue life at different temperatures.

3.2.3 Low-cycle fatigue life prediction based on total strain energy density

Under cyclic loading with a low strain, little

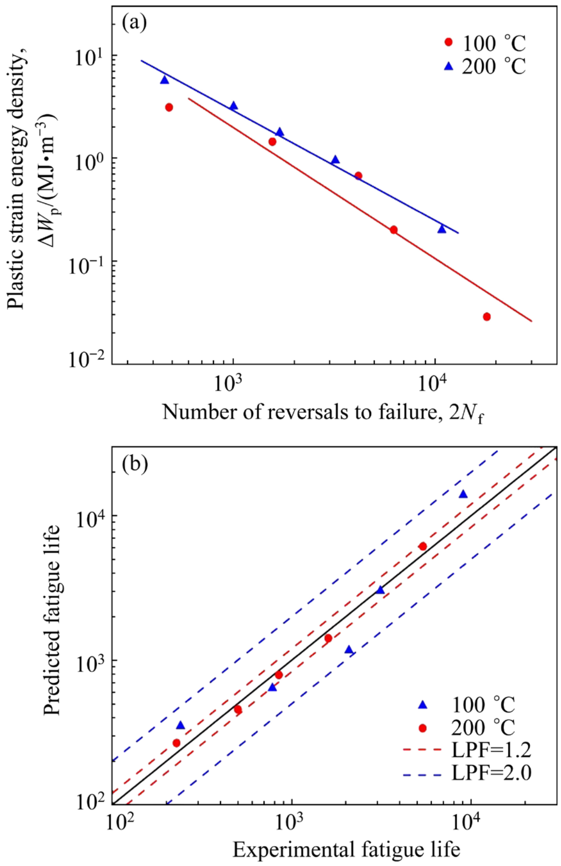

Fig. 7 Relation between plastic strain energy density and number of reversals to failure based on HW model at different temperatures (a) and comparison between predicted and experimental fatigue lives based on HW model (b)

plastic strain appears and the plastic strain energy density approaches zero. The prediction model based on plastic strain energy density is difficult to accurately predict the fatigue life of materials under this circumstance, and the influence of elastic strain on fatigue life needs to be considered. As a result, it is appropriate to adopt the total strain energy density as a fatigue life prediction parameter. The Golos−Ellyin (GE) prediction model based on total strain energy density is introduced in this work, as shown in Eq. (10):

$$\Delta W_t=\Delta W_e+\Delta W_p=K\left(2N_f\right)^a \tag{10}$$

where K and a represent the total strain energy density coefficient and exponent, respectively, and their corresponding values are shown in Table 3. ΔW_t, ΔW_p, and ΔW_e symbolize the total, plastic, and elastic strain energy density of materials, respectively, and ΔW_e is presented in Eq. (11):

$$\Delta W_e=\frac{\sigma_{max}^2}{2E}=\frac{1}{2E}\left(\frac{\Delta\sigma}{2}+\sigma_m\right)^2 \tag{11}$$

where σ_{max} and σ_m are the peak tensile stress and mean stress obtained from mid-life hysteresis loops, respectively.

Figure 8(a) shows the relation between total strain energy density and the number of reversals to failure based on the GE model. It was revealed that the fitting curves of ΔW_t−$2N_f$ were highly consistent with the corresponding experimental data at various temperatures, where the comparison is given in Fig. 8(b). The figure presents data at 100 and 200 ℃ at LPF values of 1.3 and 1.1, respectively, which were lower than those of the mentioned models.

Based on the above analysis, it was revealed that all prediction models had a better prediction accuracy at 200 ℃ than at 100 ℃. Meanwhile, at the same temperature, the LPF value of the GE model reached a minimum, suggesting that the

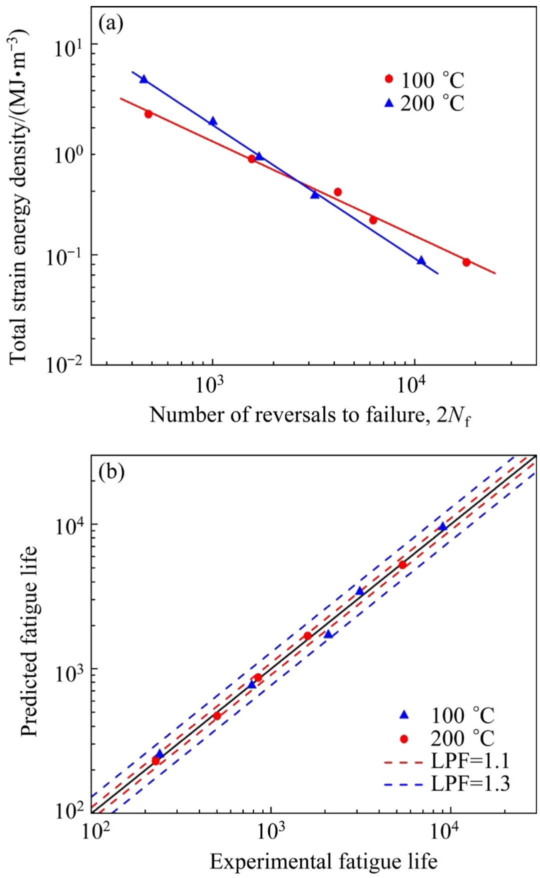

Fig. 8 Relation between total strain energy density and number of reversals to failure based on GE model at different temperatures (a) and comparison between predicted and experimental fatigue lives based on GE model (b)

model based on the total strain energy density could present a more accurate prediction compared with other models.

3.3 LCF fracture morphology

3.3.1 Fatigue fracture morphology at low strain

Figure 9 shows fatigue fracture morphology under the condition of 100 °C and the strain of 0.6%. From Fig. 9(a), it was shown that several voids of different sizes were distributed near the sample surface, leading to the stress concentration in this region. With the progress of cyclic loading, the stress concentration would be further intensified, which promoted fatigue crack initiation (FCI).

A typical fatigue crack growth zone with obvious fatigue striations is shown in Figs. 9(b, c). It was noted that the fatigue crack propagation (FCP) direction was always perpendicular to the fatigue striations, as marked by yellow arrows, and spacing between fatigue striations reflected the propagation speed. At the early stage of fatigue crack propagation, the spacing between fatigue striations was small, which meant a relatively slow propagation, as shown in Fig. 9(b). However, at the late stage of fatigue crack propagation, fatigue striations with a larger spacing were observed, indicating that the propagation process was accelerated. Meanwhile, some cracks were found to coalesce with each other, forming tear ridge bands at junctions [14], as illustrated in Fig. 9(c). In addition, a few secondary cracks parallel to fatigue striations existed in the local crack propagation area while an increase in secondary cracks was also observed with cyclic loading. The final rupture zone of the material could be seen in Fig. 9(d). The size of secondary cracks in this area increased significantly compared with that in the FCP zone. Moreover, cleavage planes of different sizes were also discovered on the fracture surface.

The fatigue fracture morphology under the condition of 200 °C and the strain of 0.6% is shown in Fig. 10. Several FCI areas were distributed on the surface and central region of fatigue samples, as illustrated in Fig. 10(a). At the early stage of the fatigue crack propagation, several dimples were observed; however, fatigue striations were not as pronounced as that at 100 °C, as shown in Fig. 10(b). When the crack propagation tended to be stable, larger cleavage planes and dimples appeared on the fracture surface, and the number of secondary cracks increased substantially, as depicted in Fig. 10(c). Figure 10(d) shows the final

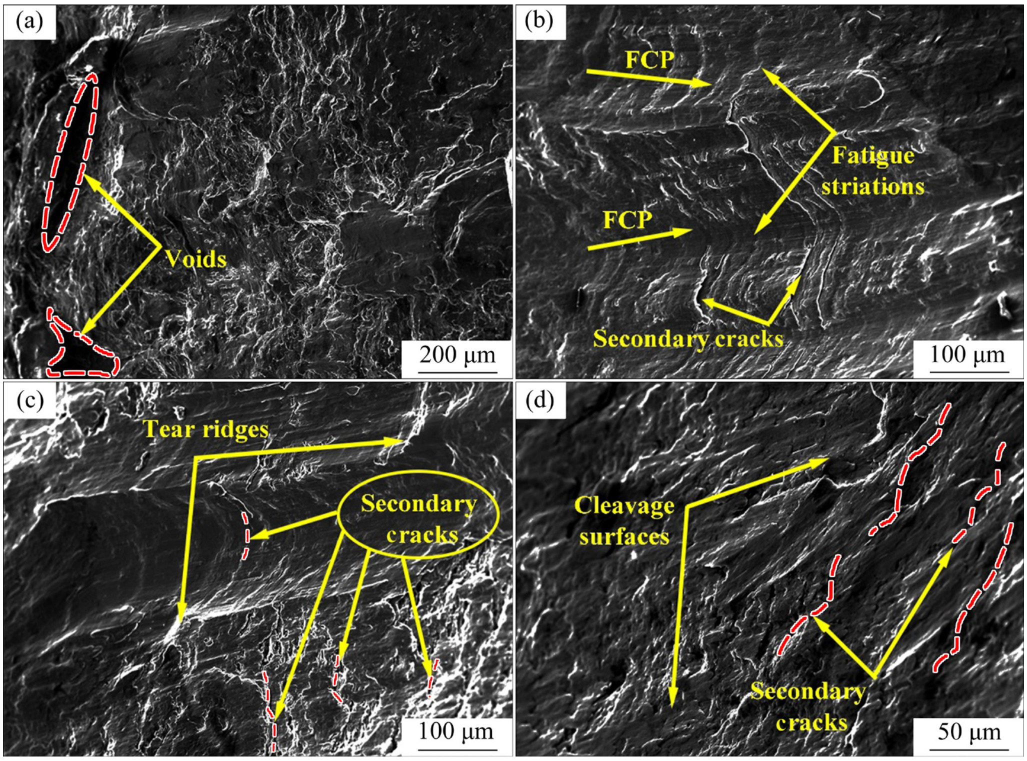

Fig. 9 Fatigue fracture morphology under condition of 100 °C and strain of 0.6%: (a) Fatigue crack initiation zone; (b, c) Fatigue crack propagation zone; (d) Final rupture zone

rupture zone, which was dominated by large-area cleavage planes and dimples, indicating a more obvious ductile fracture characteristic than that at 100 °C. In addition, some tear ridges were also observed on the local fracture surface.

3.3.2 Fatigue fracture morphology at high strain

The fatigue fracture morphology under the condition of 100 °C and the strain of 1.0% is given in Fig. 11. Multiple FCI areas were observed in Fig. 11(a). The early crack propagation zone is

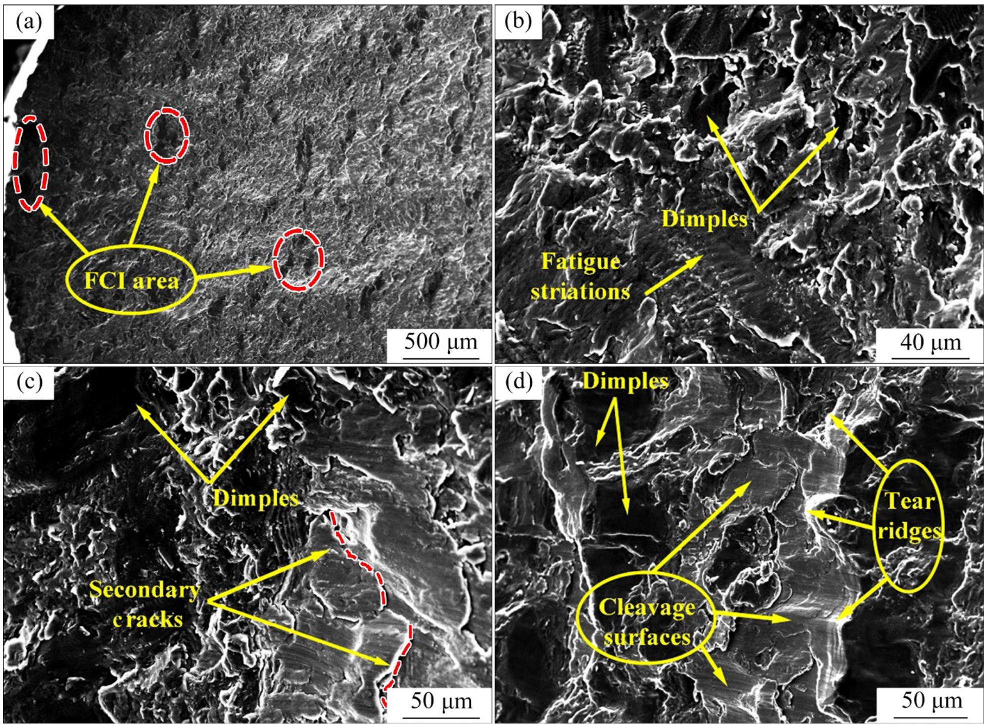

Fig. 10 Fatigue fracture morphology under condition of 200 °C and strain of 0.6%: (a) Fatigue crack initiation zone; (b, c) Fatigue crack propagation zone; (d) Final rupture zone

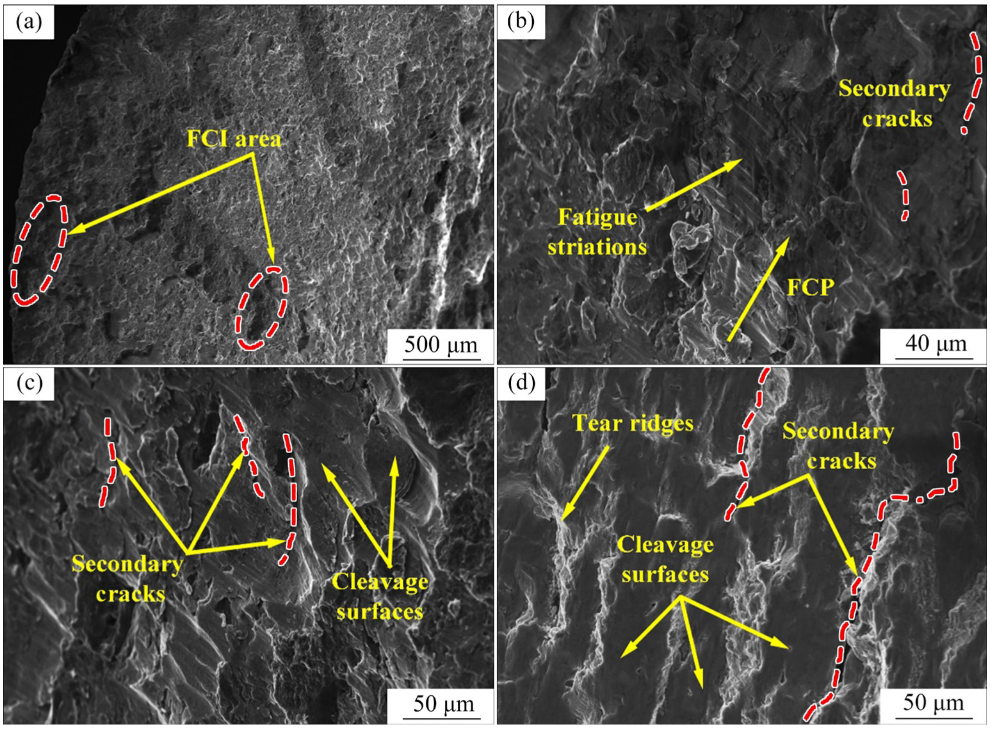

Fig. 11 Fatigue fracture morphology under condition of 100 °C and strain of 1.0%: (a) Fatigue crack initiation zone; (b, c) Fatigue crack propagation zone; (d) Final rupture zone

shown in Fig. 11(b), where weak fatigue striations could be observed and a few secondary cracks began to emerge in the local area. As the cyclic process proceeded, fatigue striations basically disappeared. On the other hand, more secondary cracks and cleavage planes were also observed, as illustrated in Fig. 11(c). Compared with Fig. 9(d), the final rupture zone in Fig. 11(d) was flatter and the area was dominated by cleavage planes and tear ridges, showing an obvious quasi-cleavage fracture characteristic. In addition, larger size secondary cracks could be also observed in the local zone.

Figure 12 shows the fatigue fracture morphology under the condition of 200 °C and the strain of 1.0%. A few oxidation inclusions on the surface of samples appeared in Fig. 12(a), resulting in the initiation of fatigue cracks. At the early stage of crack propagation, a small number of dimples and fatigue striations with an irregular shape were observed on the fracture surface, as shown in Fig. 12(b). However, at the late stage of crack propagation depicted in Fig. 12(c), fatigue striations were absent and numerous tear ridges appeared. Meanwhile, the number of dimples also increased significantly. Figure 12(d) presents the final rupture zone where obvious grain boundaries were observed, indicating a more evident grain morphology compared with Fig. 10(d). Moreover, the size and depth of dimples in Fig. 12(d) were far smaller than those in Fig. 10(d), which meant that the ductile fracture characteristic was significantly weakened.

4 Discussion

For the strain-controlled LCF tests, the fatigue life of the alloy was closely related to the temperature and strain. At the same temperature, the higher the strain was, the greater the cyclic stress was. Meanwhile, the process of fatigue crack initiation and propagation was accelerated, which reduced the fatigue life of the alloy. At the same strain, with the increase of test temperature, the thermal softening effect on the alloy was intensified, which led to an increase in fatigue crack growth rate and a decrease in fatigue life of the alloy. In the research on fatigue fracture behavior, it was necessary to pay more attention to the characteristics of fatigue striations. It was generally accepted that fatigue striations were the traces left by fatigue crack propagation, the spacing between fatigue striations represented the rate of fatigue crack propagation, and the direction of the vertical fatigue striations represented the direction

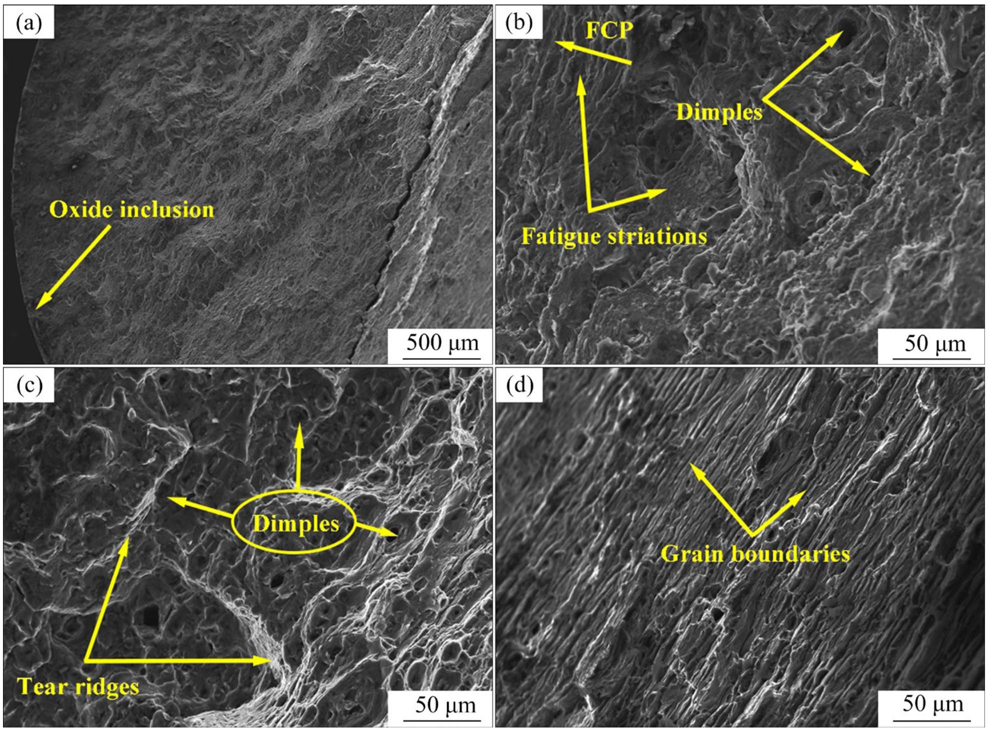

Fig. 12 Fatigue fracture morphology under condition of 200 °C and strain of 1.0%: (a) Fatigue crack initiation zone; (b, c) Fatigue crack propagation zone; (d) Final rupture zone

of fatigue crack propagation.

For aluminum alloys, the fatigue striations were usually produced by repeated plastic blunting-sharpening (B-S) due to the slip of dislocations in the plastic zone in front of the fatigue crack tips [35,36]. During cyclic loading, the fatigue crack continued to propagate, which resulted in continuous dislocation slip in the plastic zone in front of the fatigue crack tips. For the 2195 Al−Li alloy at the low temperature and strain (corresponding to the experimental conditions of 100 °C and 0.6% strain in this work), a higher fatigue life was usually observed. The fatigue fracture occurred after cyclic loading of higher cycles, which made the fatigue crack propagation time longer and the dislocation slip in the plastic zone in front of the fatigue crack tip relatively sufficient. As a result, obvious fatigue striations could be observed, as shown in Fig. 9. As the temperature and strain increased, the fatigue life of the alloy decreased obviously, and the time of fatigue crack propagation decreased, which led to the weakening of dislocation slip in the plastic zone in front of the fatigue crack tip. Therefore, relatively weak fatigue striations appeared on the fatigue fracture surface, as shown in Figs. 10 and 11. Besides, the fatigue life of 2195 Al−Li alloy was only 228 cycles under the condition of high temperature and strain (corresponding to the experimental conditions of 200 °C and 1.0% strain in this work), which was the lowest among all test conditions. So, the slip of dislocation in the plastic zone in front of the fatigue crack tips was the weakest, so the fatigue striations were difficult to be detected, as presented in Fig. 12.

For the fatigue fracture characteristics at 200 °C, the fatigue striations might be influenced by the second phase evolution as well. According to our previous research results [37], T_1 phases (Al_2CuLi), θ' phases (Al_2Cu), and intermetallic (Al_7Cu_2Fe) were main precipitates in the 2195 Al−Li alloy after T6 treatment, among which T_1 phase and θ' phase hinder the dislocation slip. When the LCF test was carried out at 200 °C, it was equivalent to prolonging the artificial aging time, which might result in an increase of the number of T_1 phase and θ' phase particles, an increase of the thickness and length of the T_1 phase, as well as the intensified retardation of dislocation slip in the plastic zone in front of fatigue crack tips. Therefore, the fatigue fracture surface at higher temperatures usually exhibited weaker fatigue striations than that at lower temperatures. In addition, when the strain is 1.0%, an obvious intergranular fracture characteristic in the final rupture zone was observed. This might be attributed to the presence of a certain width of precipitation-free zone (PFZ) near the grain boundary under the condition of higher temperatures and strains. The strength of grain boundaries was lower than that at other positions due to the presence of PFZ, which resulted in the fracture being more likely to occur at the grain boundary. As a result, the final rupture zone under the condition of 200 °C and the strain of 1.0% showed the characteristics of intergranular fracture.

5 Conclusions

(1) The cyclic stress response curve of the 2195 Al−Li alloy extruded sheet at 100 °C and strain of 0.6% exhibited complete cyclic hardening, while the cyclic response curves under other conditions showed cyclic hardening firstly followed by cyclic softening. The cyclic stress and the fatigue life at 100 °C were all higher than those at 200 °C.

(2) The fatigue life prediction models were developed based on the total strain, the plastic and total strain energy density, respectively. All fatigue life prediction models had a better prediction accuracy at 200 °C than at 100 °C, and the fatigue life prediction model based on the total strain energy density presented a more accurate prediction at the same temperature.

(3) The fatigue striations were noticeable under the condition of 100 °C and strain of 0.6%, and then gradually weakened with increasing temperature and strain. Moreover, compared with the fatigue fracture surface under other experimental conditions, the fatigue fracture morphology under the condition of 200 °C and strain of 1.0% was quite different, which exhibited an obvious intergranular fracture.

Acknowledgments

This work was supported by the National Natural Science Foundation of China (No. 51975330), the Key Research and Development Program of Shandong Province, China (No. 2021ZLGX01), and the Project of Colleges and

Universities Innovation Team of Jinan City, China (No. 2021GXRC030).

References

[1] DUAN S Y, WU C L, GAO Z, CHA L M, FAN T W, CHEN J H. Interfacial structure evolution of the growing composite precipitates in Al−Cu−Li alloys [J]. Acta Materialia, 2017, 129: 352−360.

[2] JIANG Bo, CAO Fu-hua, WANG Hai-sheng, YI Dan-qing, JIANG Yong, SHEN Fang-hua, WANG Bin, LIU Hui-qun. Effect of aging time on the microstructure evolution and mechanical property in an Al−Cu−Li alloy sheet [J]. Materials Science and Engineering: A, 2019, 740/741: 157−164.

[3] LU Ding-ding, LI Jin-feng, NING Hong, MA Peng-cheng, CHEN Yong-lai, ZHANG Xu-hu, ZHANG Kai, LI Jian-mei. ZHANG Rui-feng, Effects of microstructure on tensile properties of AA2050-T84 Al−Li alloy [J]. Transactions of Nonferrous Metals Society of China, 2021, 31: 1189−1204.

[4] TAO Xue-fei, GAO Yu-kui. Effects of wet shot peening on microstructures and mechanical properties of a 2060-T8 aluminum−lithium alloy [J]. Materials Science and Engineering: A, 2022, 832: 142436.

[5] SUN G D, ZHOU L, LIU Y N, YANG H F, JIANG J T, LI G A. Microstructure characterization and evaluation of mechanical properties in 2A97 aluminum−lithium alloys welded by stationary shoulder friction stir welding [J]. Journal of Materials Research and Technology, 2022, 16: 416−432.

[6] TANG Jian-guo, YU Bo, ZHANG Jin, XU Fu-shun, BAO Chong-jun. Effects of pre-deformation mode and strain on creep aging bend-forming process of Al−Cu−Li alloy [J]. Transactions of Nonferrous Metals Society of China, 2020, 30: 1227−1237.

[7] XU Y B, ZHANG Y, WANG Z G, HU Z Q. Fatigue and fracture behavior of aluminum−lithium alloys at ambient and cryogenic temperatures [J]. Scripta Metallurgica et Materialia, 1995, 33: 179−183.

[8] ZHANG Qing-you, ZHANG Cun-sheng, LIN Jun, ZHAO Guo-qun, CHEN Liang, ZHANG Hao. Microstructure analysis and low-cycle fatigue behavior of spray-formed Al−Li alloy 2195 extruded plate [J]. Materials Science and Engineering: A , 2019, 742: 773−787.

[9] PRASAD N E, RAO P R. Low cycle fatigue resistance of Al−Li alloys [J]. Materials Science and Technology, 2000, 16: 408−426.

[10] LIU S M, WANG Z G. Fatigue properties of 8090 Al−Li alloy processed by equal-channel angular pressing [J]. Scripta Materialia, 2003, 48: 1421−1426.

[11] LEWANDOWSKA M, MIZERA J, WYRZYKOWSKI J W. Cyclic behaviour of model Al−Li alloys: Effect of the precipitate state [J]. Materials Characterization, 2000, 45: 195−202.

[12] WANG M, PANG J C, LI S X, ZHANG Z F. Low-cycle fatigue properties and life prediction of Al−Si piston alloy at elevated temperature [J]. Materials Science and Engineering: A, 2017, 704: 480−492.

[13] BROWN L B, JONES J L, LOCKE J S, BURNS J T. Effect of low temperature, low water vapor pressure environments on the fatigue behavior of an Al−Li aerospace alloy [J]. International Journal of Fatigue, 2021, 148: 106215.

[14] GUO Bing-bin, ZHANG Wei-zheng, LI Shao-guang, WANG Xiao-song. High temperature low cycle fatigue and creep-fatigue behavior of a casting Al−9Si−Cu−Mg alloy used for cylinder heads [J]. Materials Science and Engineering: A, 2017, 700: 397−405.

[15] JOYCE M R, STARINK M J, SINCLAIR I. Assessment of mixed mode loading on macroscopic fatigue crack paths in thick section Al−Cu−Li alloy plate [J]. Materials & Design, 2016, 93: 379−387.

[16] MOREIRA P M G P, de JESUS A M P, de FIGUEIREDO M A V, WINDISCH M, SINNEMA G, de CASTRO P M S T. Fatigue and fracture behaviour of friction stir welded aluminium–lithium 2195 [J]. Theoretical and Applied Fracture Mechanics, 2012, 60: 1−9.

[17] METZ D F, BARKEY M E. Fatigue behavior of friction plug welds in 2195 Al−Li alloy [J]. International Journal of Fatigue, 2012, 43: 178−187.

[18] DE P S, MISHRA R S, BAUMANN J A. Characterization of high cycle fatigue behavior of a new generation aluminum lithium alloy [J]. Acta Materialia, 2011, 59: 5946−5960.

[19] HATAMLEH O, HILL M, FORTH S, GARCIA D. Fatigue crack growth performance of peened friction stir welded 2195 aluminum alloy joints at elevated and cryogenic temperatures [J]. Materials Science and Engineering: A, 2009, 519: 61−69.

[20] LAFFIN C, RAGHUNATH C R, LOPEZ H F. Hydrogen induced surface cracking in an 8090 Al−Li alloy during high cycle fatigue [J]. Scripta Metallurgica et Materialia, 1993, 29: 993−998.

[21] GANESH SUNDARA RAMAN S, RADHAKRISHNAN V M. On cyclic stress–strain behaviour and low cycle fatigue life [J]. Materials & Design, 2002, 23: 249−254.

[22] KLIMAN V, BÍLÝ M. Hysteresis energy of cyclic loading [J]. Materials Science and Engineering, 1984, 68: 11−18.

[23] GOLOS K, ELLYIN F. A total strain energy density theory for cumulative fatigue damage [J]. Journal of Pressure Vessel Technology, 1988, 110: 36−41.

[24] WANG M, PANG J C, ZHANG M X, LIU H Q, LI S X, ZHANG Z F. Thermo-mechanical fatigue behavior and life prediction of the Al−Si piston alloy [J]. Materials Science and Engineering: A, 2018, 715: 62−72.

[25] ZHANG Peng, ZHU Qiang, CHEN Gang, QIN He-yong, WANG Chuan-jie. Grain size based low cycle fatigue life prediction model for nickel-based superalloy [J]. Transactions of Nonferrous Metals Society of China, 2018, 28: 2102−2106.

[26] HE Guo-ai, LI Kai, YANG Yong, LIU Yu, WU Wen-ke, HUANG Cheng. Effect of heat treatment on the microstructure and mechanical properties of cryogenic rolling 2195 Al−Cu−Li alloy [J]. Materials Science and Engineering: A, 2021, 822: 141682.

[27] MA Yun-long, LI Jin-feng, ZHANG Run-zhe, TANG Jian-guo, HUANG Cheng, LI Hong-ying, ZHENG Zi-qiao. Strength and structure variation of 2195 Al−Li alloy caused by different deformation processes of hot extrusion and

cold-rolling [J]. Transactions of Nonferrous Metals Society of China, 2020, 30: 835−849.
[28] LI Q, NING J, CHEN L, HU J L, LIU Y X. The mechanical response and microstructural evolution of 2195 Al−Li alloy during hot tensile deformation [J]. Journal of Alloys and Compounds, 2020, 848: 156515.
[29] ZHOU C, ZHAN L H, LI H, ZHAO X, CHEN F, HUANG M H. Creep ageing behaviour assisted by electropulsing under different stresses for Al−Cu−Li alloy [J]. Transactions of Nonferrous Metals Society of China, 2021, 31: 1916−1929.
[30] NIU Peng-liang, LI Wen-ya, YANG Cheng-gang, CHEN Yu-hua, CHEN Dao-lun. Low cycle fatigue properties of friction stir welded dissimilar 2024-to-7075 aluminum alloy joints [J]. Materials Science and Engineering: A, 2022, 832: 142423.
[31] ESWARA PRASAD N, VOGT D, BIDLINGMAIER T, WANNER A, ARZT E. High temperature, low cycle fatigue behaviour of an aluminium alloy (Al–12Si–CuMgNi) [J]. Materials Science and Engineering: A, 2000, 276: 283−287.
[32] ABDALLA J A, HAWILEH R A, OUDAH F, ABDELRAHMAN K. Energy-based prediction of low-cycle fatigue life of BS 460B and BS B500B steel bars [J]. Materials & Design, 2009, 30: 4405−4413.
[33] ZHANG Q, ZUO Z X, LIU J X. High-temperature low-cycle fatigue behaviour of a cast Al−12Si−CuNiMg alloy [J]. Fatigue & Fracture of Engineering Materials & Structures, 2013, 36: 623−630.
[34] SONG M S, KONG Y Y, RAN M W, SHE Y C. Cyclic stress–strain behavior and low cycle fatigue life of cast A356 alloys [J]. International Journal of Fatigue, 2011, 33: 1600−1607.
[35] SHAHA S K, CZERWINSKI F, KASPRZAK W, FRIEDMAN J, CHEN D L. Effect of Mn and heat treatment on improvements in static strength and low-cycle fatigue life of an Al−Si−Cu−Mg alloy [J]. Materials Science and Engineering: A, 2016, 657: 441−452.
[36] FAN K L, HE G Q, LIU X S, LIU B, SHE M, YUAN Y L, YANG Y, LU Q. Tensile and fatigue properties of gravity casting aluminum alloys for engine cylinder heads [J]. Materials Science and Engineering: A, 2013, 586: 78−85.
[37] ZHANG Cun-sheng, LIU Ming-fu, MENG Zi-jie, ZHANG Qing-you, ZHAO Guo-qun, CHEN Liang, ZHANG Hao, WANG Jia. Microstructure evolution and precipitation characteristics of spray-formed and subsequently extruded 2195 Al−Li alloy plate during solution and aging process [J]. Journal of Materials Processing Technology, 2020, 283: 116718.

2195 铝锂合金的温热低周疲劳行为和疲劳寿命预测

孟子杰[1]，张存生[1]，吴承格[2]，张 豪[3]，陈 良[1]，赵国群[1]，闫 海[2]

1. 山东大学 材料液固结构演化与加工教育部重点实验室，济南 250061；
2. 山东交通学院 工程机械学院，济南 250357；
3. 江苏豪然喷射成形合金有限公司，镇江 212009

摘 要：为研究 2195 铝锂合金在温热条件下(100 和 200 ℃)的低周疲劳行为，首先进行应变控制的低周疲劳试验。结果表明，合金的起始和中值寿命滞回环均呈现中心对称特征。在 100 ℃、应变幅值为 0.6%条件下的循环应力响应曲线表现出完全循环硬化特征，而其他条件下的循环应力响应曲线均呈先循环硬化、然后循环软化的循环特征。随后，采用多种低周疲劳寿命预测模型对 2195 铝锂合金疲劳寿命进行评价。结果表明，基于总应变能密度的寿命预测模型具有最佳的预测精度。最后，为揭示 2195 铝锂合金的疲劳断裂机理，对不同试验条件下合金的疲劳断口进行观察。结果表明，在 100 ℃、应变幅值为 0.6%的条件下，合金断面上的疲劳条纹十分明显，但随着试验温度和应变幅值的升高，合金断面上的疲劳条纹逐渐弱化。在温度为 200 ℃、应变幅值为 1.0%条件下的疲劳断口呈明显沿晶断裂特征。

关键词：2195 铝锂合金；低周疲劳行为；疲劳寿命预测；疲劳断裂行为

(Edited by Wei-ping CHEN)